

## Role of size on the relative importance of fluid dynamic losses in linear cryocoolers

Carl Kirkconnell<sup>a</sup>, Ali Ghavami<sup>b</sup>, S. Mostafa Ghiaasiaan<sup>b</sup>, Matthew Perrella<sup>b</sup>

<sup>a</sup>West Coast Solutions, 6741 Brentwood DR, Huntington Beach, CA, USA 92648;

<sup>b</sup>Georgia Institute of Technology, G.W. Woodruff School of Mechanical Engineering, Atlanta, GA, 30332

carlk@wecoso.com

**Abstract.** Thermodynamic modeling results for a novel small satellite (SmallSat) Stirling Cryocooler, capable of delivering over 200 mW net cooling power at 80 K for less than 6 W DC input power, are used in this paper as the basis for related pulse tube computational fluid dynamics (CFD) analysis. Industry and government requirements for SmallSat infrared sensors are driving the development of ever-more miniaturized cryocooler systems. Such cryocoolers must be extremely compact and lightweight, a challenge met by this research team through operating a Stirling cryocooler at a frequency of approximately 300 Hz. The primary advantage of operating at such a high frequency is that the required compression and expansion swept volumes are reduced relative to linear coolers operating at lower frequencies, which evidently reduces the size of the motor mechanisms and the thermodynamic components. In the case of a pulse tube cryocooler, this includes a reduction in diameter of the pulse tube itself. This unfortunately leads to high boundary layer losses, as the presented results demonstrate. Using a Stirling approach with a mechanical moving expander piston eliminates this small pulse tube loss mechanism, but other challenges are introduced, such as maintaining very tight clearance gaps between moving and stationary elements. This paper focuses on CFD modelling results for a highly miniaturized pulse tube cooler.

### 1. Introduction

Highly miniaturized cryocoolers are required for the successful deployment of high performance infrared sensors on small satellites (SmallSats). Applications include Earth imaging, imaging of other planetary bodies, space situational awareness, and capability augmentation for robotics missions, just to name a few. This research aggressively seeks to address SmallSat applications all the way down to a 3U (10 x 10 x 30 cm) satellite.

The present concept design is depicted in figure 1. The targeted low end temperature is 80K with an efficiency target of >10% Carnot, which is aggressive for a cooler of this physical size and operating point. A Stirling approach has been selected based upon the better results achieved to date by miniature Stirling coolers in this temperature range as compared to miniature pulse tubes [1, 2, 3, 4, 5]. The component sizing depicted in the solid model is based upon a thermodynamic model with a drive frequency of 300 Hz as discussed in an earlier paper by this same research team [6].



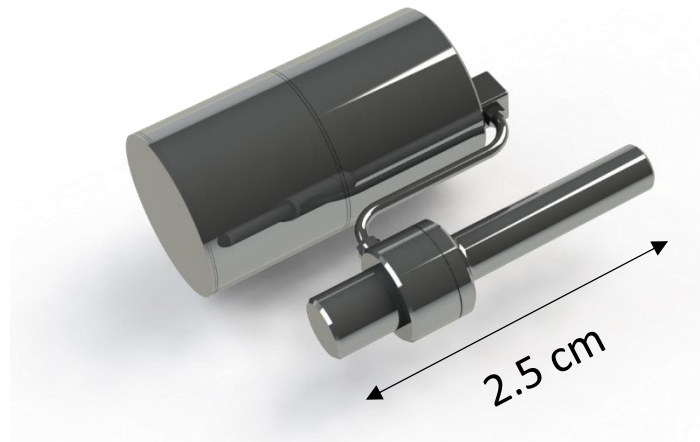


**Figure 1.** Solid model concept design for the SmallSat Stirling Cryocooler (SSC). Shown as a single-piston compressor with a “passive” Stirling expander (i.e., no expander motor). Overall size based upon initial thermodynamic modeling results [6].

The operating frequency of the SSC is well in excess of the 60-100 Hz characteristic of current state of the art in miniature Stirling coolers, and even well beyond the 90-140 Hz range recently reported by Lockheed Martin for the pulse tube Microcryocooler [5]. The SSC compressor will clearly require innovation beyond traditional Oxford-class, flexure-based systems. The Stirling poses additional challenges by introducing moving mechanisms into the expander, as opposed to a pulse tube. Although the literature appears compelling in support of Stirling and the initial Sage modeling is promising as previously reported, this is a non-trivial complication, one warranting additional analysis.

This paper is envisioned as the first of a two-part computational fluid dynamics (CFD) study to analyze and ultimately compare the losses in miniature pulse tube and Stirling cryocoolers, with this first part focusing on the pulse tube. A systematic study has been undertaken to characterize and quantify the thermal and fluidic flow patterns inside high frequency (300 Hz) pulse tubes, starting with a meso-scale 10 mm diameter pulse tube down to 1 mm, which is at the low end of the pulse tube diameters contemplated for this application. The results show the increasing influence of detrimental boundary layer effects as the diameter of the pulse tube gets smaller.

## 2. Computation fluid dynamics study on Pulse Tubes

CFD analysis of a pulse tube expander was performed to investigate the role of size on refrigeration losses inside the pulse tube component itself. As the pulse diameter shrinks, the boundary layer region becomes an increasing percentage of the overall cross section, ultimately compromising the simplified 1-D “gas piston” assumption to the point where the pulse tube no longer functions as a practical refrigeration device. This analysis was performed to explore where that occurs, starting from a diameter of 10 mm and going down to 1 mm. The computational domain was constructed to focus on this pulse tube boundary layer loss mechanism; regenerator and other losses were not considered for this study.

### 2.1. Model setup and assumptions

The model setup and basic assumptions are provided in figure 2 and table 1. Operating conditions (i.e., refrigeration and rejection temperatures, frequency, mean pressure, etc.) representative of the target cooler based on the earlier Sage modeling of the Stirling variant were selected and fixed for the four different pulse tube sizes modeled. Typical pulse tube aspect ratio ( $L/D = 10$ ) and phase angles were selected and fixed. The heat exchangers at the ends of the pulse tube are somewhat arbitrary with design

points selected to provide the desired representative boundary conditions (isothermal with uniform velocity for flow entering the pulse tube) and again held constant between the cases so that the relative influence of pulse tube size, the focus of this study, could be isolated from other effects.

**Table 1.** Model assumptions and boundary conditions.

working gas	Helium
frequency (f)	300 Hz (sinusoid)
cold end temperature (Tcold)	80K
hot end temperature (Thot)	300K
mean pressure (Pmean)	1.54 – 1.59 MPa (*)
mass flow rate-to-pressure phase at hot end	0°
mass flow rate cold-to-mass flow rate hot phase	30° (cold end leading)
pulse tube diameter	D
pulse tube length	L
pulse tube aspect ratio (L/D)	10
heat exchanger diameters	D
heat exchanger lengths	0.3L
heat exchanger viscous resistance	7.435e8 m <sup>-2</sup>
heat exchanger inertial resistance	8147 m <sup>-1</sup>
heat exchanger porosity	0.68

(\*) Mean pressure varies slightly because it is not explicitly specified, rather it is derived to yield the objective gas column size, as described below.

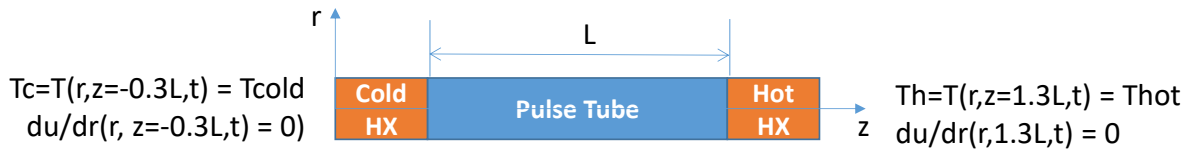


**Figure 2.** Computational domain and bounding temperature and velocity gradient conditions.

The final consideration for model setup is the mass flow rate amplitude to impose at the ends of the computational domain. The flow amplitudes were normalized based on the pulse tube size such that the percentage of gas volume displaced at each end of the tube during each half-cycle equates to approximately 25% of the total pulse tube volume, i.e., a nominal “gas piston” equal to 75% of the physical pulse tube volume, which is typical in a pulse tube cooler. This is shown mathematically by,

$$dV = dV_c = dV_h = 0.25V_{pt} = 0.25 \frac{\pi D^2}{4} L \quad (1)$$

$$dM_c = \frac{dV \times P_{mean}}{R \times T_{cold}} \quad (2)$$

$$dM_h = \frac{dV \times P_{mean}}{R \times T_{hot}} \quad (3)$$

$$|m_{cold}| = \sqrt{2} \frac{dM_c}{dt} = \sqrt{2} \times dM_c \times 2f \quad (4)$$

$$|m_{hot}| = \sqrt{2} \frac{dM_h}{dt} = \sqrt{2} \times dM_h \times 2f \quad (5)$$

## 2.2. Numerical Solution

A 2-D axisymmetric analysis was performed in ANSYS 17.1, neglecting gravity and other body forces. The computational domain was divided into 480 axial elements (300 for the pulse tube and 90 for each heat exchanger) by 50 radial elements, with finer mesh at the wall as defined by the factor of 2 bias in the radial direction (i.e.,  $\Delta r$  at the wall is one half  $\Delta r$  along the centerline). The system is in periodic steady state when cyclic variations of all parameters become identical repetitions. All our simulations have shown that periodic steady state is achieved after about 100 cycles, as illustrated in figure 3. 130 cycles were performed to ensure that periodic steady state was achieved.

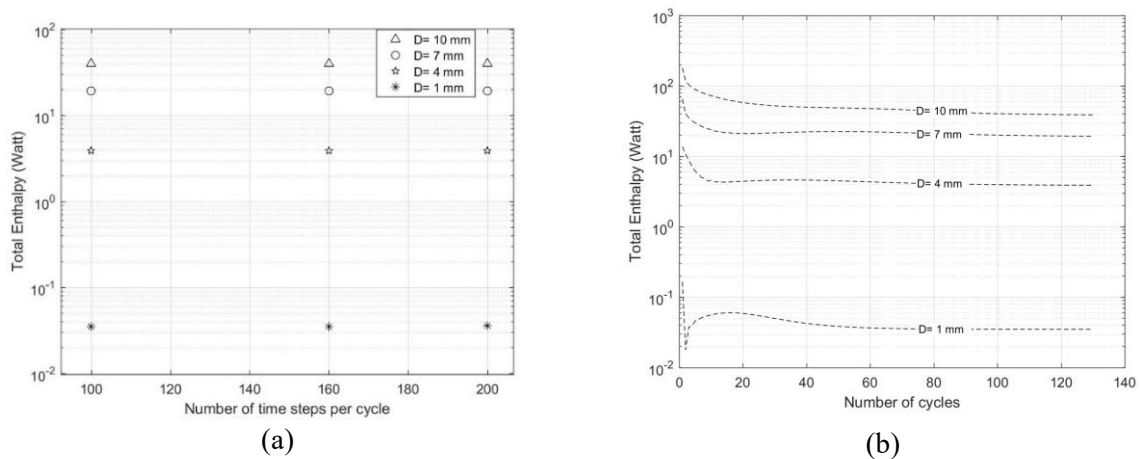


**Figure 3.** Convergence of the simulations. a) The effect of number of time steps per cycle on the predicted total enthalpy flux. b) The effect of number of cycles on the cycle-average enthalpy flux.

The pulse tube pressure containment vessel is taken as infinitesimally thin, i.e., no axial conduction. The pulse tube wall is adiabatic, while the heat exchanger walls are held constant at the respective  $T_{cold}$  and  $T_{hot}$  boundary conditions. The bounding fluid temperatures at the ends of the cold and hot heat exchangers are also held constant at  $T_{cold}$  and  $T_{hot}$ , respectively. The mass flow rates are pure sinusoids at the phase offset indicated in table 1; the amplitudes are provided below in table 2 per equations 1-5. The resulting pressure ratio at the midpoint of the pulse tube between the two bounding heat exchangers is also included in table 2, together with  $P_{mean}$  showing consistent pressure conditions between the four cases. Of critical importance is that table 2 further illustrates the proper normalization of the cases so that valid comparisons between the resulting solutions can be made.

**Table 2.** Summary of the four cases.

PT Length (L) [mm]	PT Diameter (D) [mm]	$ m_{cold} $ [g/s]	$ m_{hot} $ [g/s]	$P_{mean}$ [MPa]	$Pr_{pt} = P_{max}/P_{min}$
100	10	18.049	4.813	1.54	1.100
70	7	6.191	1.651	1.54	1.125
40	4	1.155	3.080E-1	1.56	1.137
10	1	1.805E-2	4.813E-3	1.59	1.135

## 2.3. Results

**2.3.1. Contour plots and profiles.** The qualitative nature of the resulting temperature and velocity solutions can be observed in the contour plots provided in figures 4 and 5. For the purpose of illustration, a time step was selected corresponding to the peak mass flow rate into the cold end of the computational

domain, i.e., flow to the right given the orientation of the figures. For all cases, the top edge is the pulse tube wall and the bottom edge the centerline, recalling that these are 2-D axisymmetric solutions. Starting with the temperature solutions in figure 4, the increasing influence of the boundary layer as the pulse tube diameter decreases is evident. For the 10 mm case, plug flow with minimal axial mixing is observed. The 7 mm case exhibits a mild increase in boundary layer influence with increasing evidence at 4 mm and a dominant influence at 1 mm.

Figure 5 depicts the axial velocity contours at the time step corresponding to temperature solutions in figure 4. For figure 5 the calculated velocity values were normalized by the maximum velocity occurring within the particular pulse tube at the time step shown so a common scale could be used to better illustrate the differing flow field characteristics. Here, the influence of the boundary layer is more subtle, but nevertheless still apparent. Whereas the velocity at this instant in time is fairly constant throughout the flow domain for the larger pulse tubes, the influence of drag along the wall affecting a larger percentage of the cross section can be seen in the smallest pulse tube, becoming more prominent in the direction of the flow, which is the direction of boundary layer growth.

This growth in the velocity boundary thickness layer relative to the diameter of the pulse tube is shown more clearly in the velocity profiles depicted in figure 6. Again for this same instant in time, the normalized velocity profiles are provided for all four pulse tubes at two different axial locations. The 10 mm and 7 mm diameter tube solutions are nearly coincident, while the 4 mm solution diverges as the boundary layer becomes nontrivial, and a dramatically divergent 1 mm solution reveals that the maximum velocity is no longer even occurring along the centerline due to boundary layer effects.

Temperature profiles for the cold and hot region ( $L/4$  and  $3L/4$ , respectively) are provided in figure 7. Once again, the 10 mm and 7 mm cases are very similar; there is no discernible evidence in this data of a fundamental difference in the qualitative fluid dynamics solutions for these cases. There is clearly an increasing influence on the thermal boundary layer thickness for the 4 mm case, yet the core flow characteristic is essentially the same as the two larger pulse tubes. The 1 mm case solution, on the other hand, yields a clearly distinct temperature profile. There is greater radial variation in the temperature at each axial location, and there is a distinct minimum in the temperature profile occurring well away from the wall, at approximately  $r^* = 0.8$ . The result is warmer temperature in the cold region and a mix of colder and warmer temperature in the hot region for the 1 mm pulse tube, indicating increased axial mixing, which is well known to lead to losses in pulse tube refrigeration efficiency.

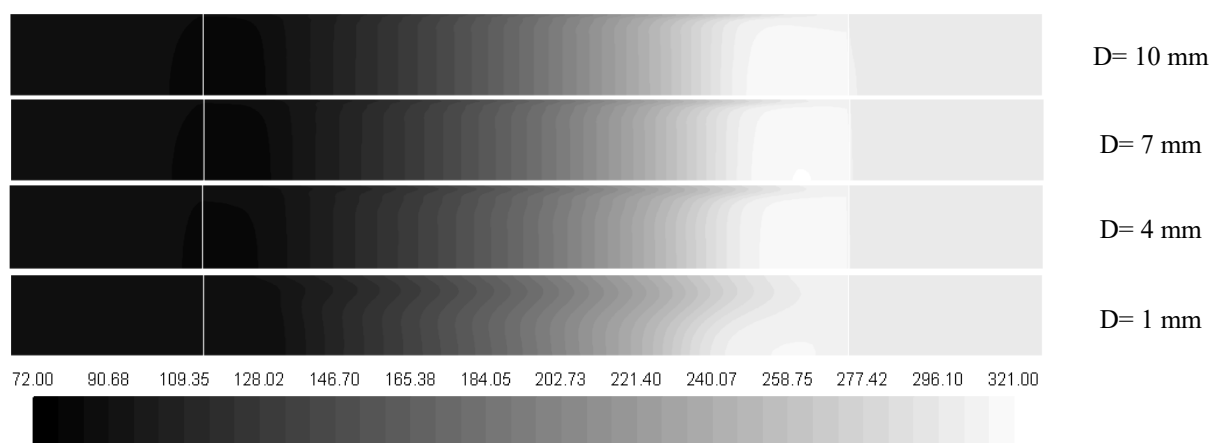


**Figure 4.** Temperature contours at  $t^* = 0.25$ . Boundary layer effects become more prominent for smaller pulse tube size as revealed by radial variations in the temperature solution. Note: faint white lines depict the boundaries of the pulse tube relative to the heat exchangers.

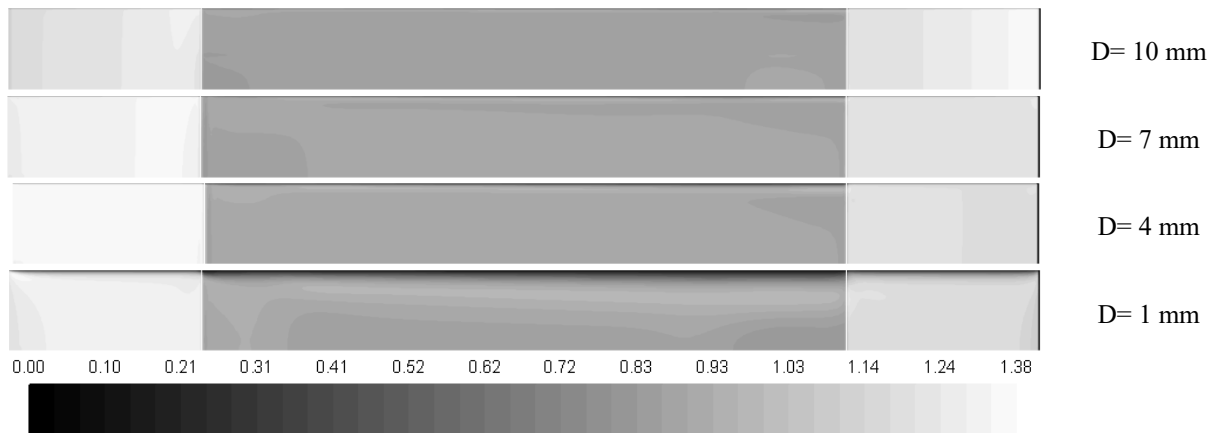


**Figure 5.** Axial velocity contours at  $t^* = 0.25$ . Boundary layer effects again more prominent for smaller pulse tubes, especially towards the hot end, which is in the direction of flow for this time step. Note: highest local velocities occur within the heat exchangers because of the constricted flow area due to the presence of the heat exchanger matrices.

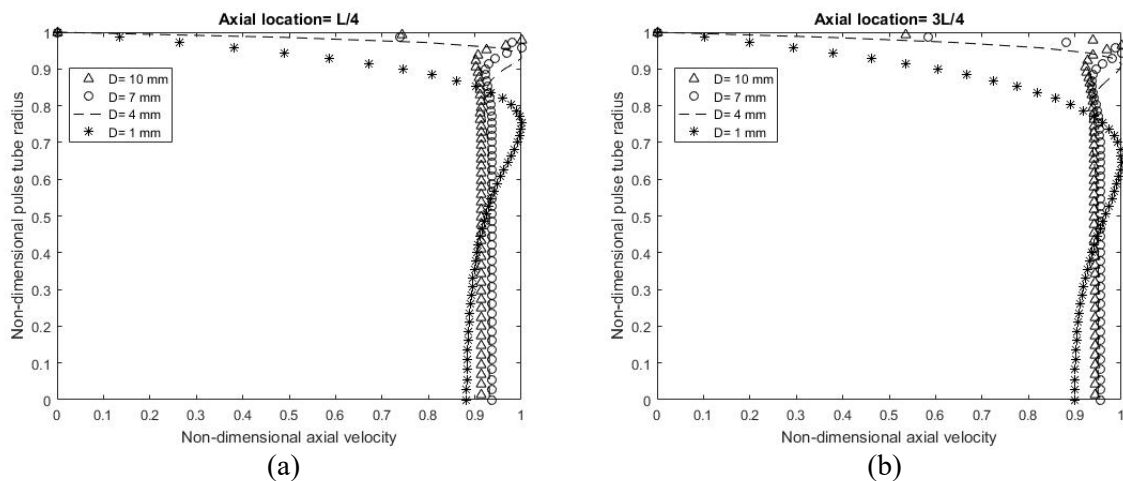


**Figure 6.** Axial velocity profiles. (a)  $L/4$ , cold region; (b)  $3L/4$ , hot region.

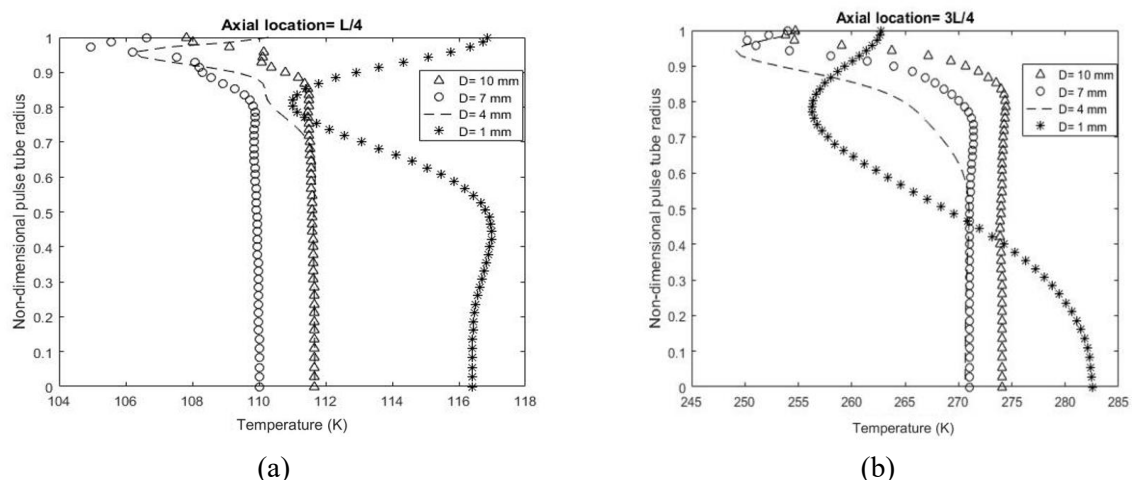


**Figure 7.** Temperature profiles. (a)  $L/4$ , cold region; (b)  $3L/4$ , hot region. Note the presence of substantially warmer gas in cold region and mixture of cold and warm gas in warm region for 1 mm case, indicative of increased axial mixing.



**2.3.2. Quantitative assessment.** Figures 4 through 7 clearly show the increasing role of boundary layer effects on the solution to the governing equations, but what is primarily of interest is how these boundary layer effects influence the refrigeration efficiency of the pulse tube. Further, it would be noted that all of the prior plots are for one particular instant in time. Quantifying the cycle-averaged influence requires additional analysis.

Consider the plots of standard deviation of the temperature solution in figure 8, shown at the same three axial locations depicted in figures 6 and 7. Now, we are looking at the entire operating cycle, so the data describe the entire cyclical performance rather than just a snapshot in time. The standard deviation quantifies the radial variability in the temperature profile, with large values indicating a greater departure from the ideal one-dimensional “gas piston” behavior. At all three time steps, the values calculated for the smallest (1 mm) pulse tube are dramatically larger than for the other three pulse tubes, quantifying the much larger radial variation in temperature in that case. Even so, it is observed that the values are distinctly lowest for the largest pulse tube with a clear and consistent increase as the pulse tube diameter shrinks at every time step and for all three axial locations.

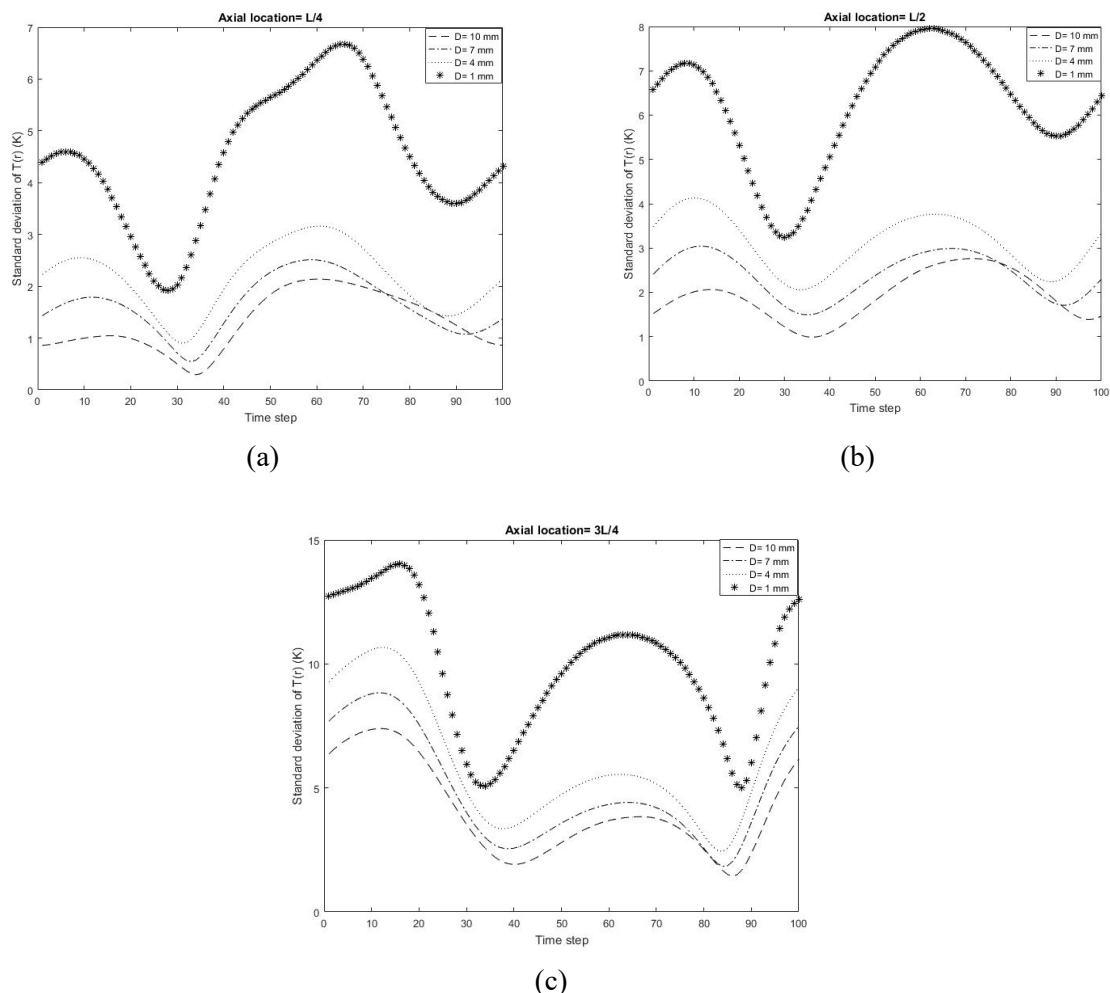


**Figure 8.** Standard deviation in the temperature solution. (a) L/4; (b) L/2; (c) 3L/4. Larger values indicate greater deviation from one-dimensional solution, which in turn indicated larger pulse tube losses.

One can demonstrate the effect of miniaturization on refrigeration performance by defining an efficiency,  $\eta$ , as the ratio between cycle-average enthalpy transport rate and input PV power per cycle,

$$\eta = \frac{\langle \dot{H} \rangle}{\langle P\dot{V} \rangle}$$

where

$$\langle \dot{H} \rangle = \frac{\int_{\text{cycle}} \left( \int_{A_{cs}} \rho v_{\text{axial}} \left( h + \frac{1}{2} |v|^2 \right) dA \right) dt}{T} = \frac{\int_{\text{cycle}} \left( \int_0^{D/2} \rho v_{\text{axial}} \left( h + \frac{1}{2} |v|^2 \right) 2\pi r dr \right) dt}{T} \quad (6)$$

$$\langle P\dot{V} \rangle = \frac{1}{2} RT_c \left( \frac{P_1}{P_0} \right) |\dot{m}_{\text{cold}}| \cos \theta \quad (7)$$

where  $\theta$  is the phase angle between cold and warm end mass flow rates. Figure 9 displays the efficiencies for the simulated pulse tubes. The deleterious effect of miniaturization is evident. For the two largest pulse tubes the boundary layer thickness is negligibly small in comparison with the pulse tube diameter, and as a result the efficiencies for the 10 mm and 7 mm diameter pulse tubes are essentially the same. For the two smaller tubes, however, the efficiency is reduced drastically.

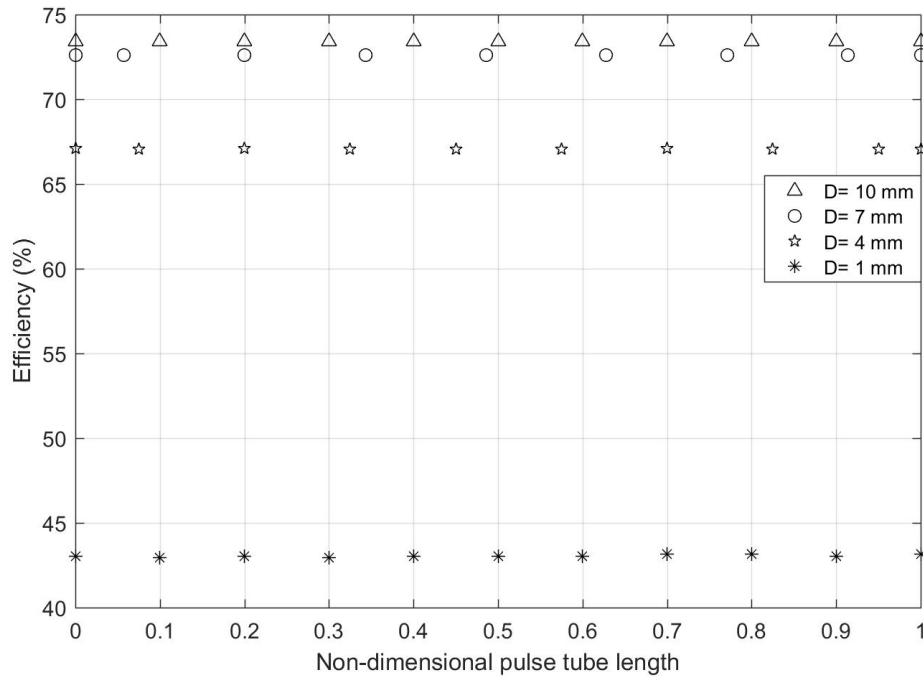


**Figure 9.** The effect of miniaturization on pulse tube efficiency.

### 3. Discussion

The targeted gross capacity for the SSC is around 500 mW to yield the objective >200 mW net refrigeration, after consideration for conduction and regenerator losses. In the case of a pulse tube cooler, “gross capacity” translates to the net total enthalpy transport capacity of the pulse tube. Past studies by this research group indicate that, absent extreme boundary layer losses, this would require a 2 to 3 mm diameter pulse tube. The results of this study seem to confirm that range, for the enthalpy transport in the 1 mm pulse tube is only 35 mW, but it would be about 400 mW if the pulse tube efficiency were comparable to the larger 7 and 10 mm pulse tubes. With these considerations, a pulse tube variant of the



SSC is clearly in the size range where extreme pulse tube boundary layer-induced losses are a major concern.

Analogous to the pulse tube boundary layer loss, a Stirling cold finger exhibits a “shuttle loss” arising from the motion of the cryogenic displacer piston within a fixed cylinder, resulting in instantaneous radial differences in the local temperature of the displacer and its cylinder, which in turn drives radial thermal transport and ultimately a “shuttling” of heat from the warm end to the cold end. The next step in this research is to use these same analysis tools to quantify Stirling shuttle loss as a function of cold finger size to explore whether highly miniaturized Stirlings exhibit a trend similar to pulse tubes. This study shows that the pulse tube boundary layer loss is fundamental, arising directly from the fluidic motion essential to the refrigeration process. Our expectation is that there may be engineering solutions involving geometry (i.e., stroke length, clearance gap) and material selection (cylinder and displacer) to mitigate the Stirling shuttle loss, which will result in a more efficient Stirling expander at this size scale than is possible with a pulse tube. This premise is presently being explored by the West Coast Solutions – Georgia Tech research team in a companion study.

#### 4. Conclusion

A CFD study has been performed to explore the role of pulse tube size on pulse tube efficiency, in particular the increasing (detrimental) role of boundary layer effects on enthalpy transport capacity as the diameter of the pulse tube gets smaller. For the frequency and pressure range of interest, pulse tube efficiency begins to drop off dramatically somewhere around 7 mm, which means that pulse tubes sized for the small satellite application are highly likely to exhibit intolerably large boundary layer induced losses.

The SmallSat Stirling Cryocooler was recently selected by NASA for a Phase I SBIR, an effort that is underway as of this writing. The aforementioned Stirling-focused analogous modeling efforts are a primary focus of the recently-commenced Phase I effort.

#### 5. References

- [1] [http://www.aim-ir.com/fileadmin/files/Data\\_Sheets\\_Cooler/2014\\_neu/2014\\_AIM\\_SX030\\_engl.pdf](http://www.aim-ir.com/fileadmin/files/Data_Sheets_Cooler/2014_neu/2014_AIM_SX030_engl.pdf)
- [2] <http://www.ricor.com/products/split-linear/k527/>
- [3] Willems D, Arts R, de Jonge G, Mullie J, and Benschop T 2016 Miniature Stirling Cryocoolers at Thales Cryogenics: Qualification Results and Integration Solutions *Cryocoolers 19* (International Cryocooler Conference, Boulder, CO) pp 85-93
- [4] [http://www.aim-ir.com/fileadmin/files/Data\\_Sheets\\_Cooler/Datasheet\\_SX040.pdf](http://www.aim-ir.com/fileadmin/files/Data_Sheets_Cooler/Datasheet_SX040.pdf)
- [5] Nast T, Olson J, Champagne P, Roth E, Saito E, Loung V, McCay B, Kenton A, and Dobbins C 2016, Development of Microcryocoolers for Space and Avionics Applications, *Cryocoolers 19* (International Cryocooler Conference, Boulder, CO) pp 65-74
- [6] Kirkconnell C, Hon R, Perrella M, Crittenden T, and Ghiaasiaan S M 2017 Development of a miniature Stirling cryocooler for LWIR small satellite applications *Proc. of SPIE* **10180**

#### Acknowledgments

This work was funded as a West Coast Solutions Internal Research and Development (IRAD) project with additional support provided by the Georgia Tech Cryo Lab (GTCL).